The Influence of Cloud and Surface Properties on the Arctic Ocean Shortwave Radiation Budget in Coupled Models*

IRINA V. GORODETSKAYA+
Lamont-Doherty Earth Observatory, and Department of Earth and Environmental Science, Columbia University, Palisades, New York

L.-BRUNO TREMBLAY
Department of Atmospheric and Oceanic Sciences, McGill University, Montreal, Quebec, Canada

BEATE LIEPERT
Lamont-Doherty Earth Observatory, Columbia University, Palisades, New York

MARK A. CANE
Lamont-Doherty Earth Observatory, and Department of Earth and Environmental Science, Columbia University, Palisades, New York

RICHARD I. CULLATHER
Lamont-Doherty Earth Observatory, Columbia University, Palisades, New York

(Manuscript received 31 July 2006, in final form 16 July 2007)

ABSTRACT

The impact of Arctic sea ice concentrations, surface albedo, cloud fraction, and cloud ice and liquid water paths on the surface shortwave (SW) radiation budget is analyzed in the twentieth-century simulations of three coupled models participating in the Intergovernmental Panel on Climate Change Fourth Assessment Report. The models are the Goddard Institute for Space Studies Model E-R (GISS-ER), the Met Office Third Hadley Centre Coupled Ocean–Atmosphere GCM (UKMO HadCM3), and the National Center for Atmosphere Research Community Climate System Model, version 3 (NCAR CCSM3). In agreement with observations, the models all have high Arctic mean cloud fractions in summer; however, large differences are found in the cloud ice and liquid water contents. The simulated Arctic clouds of CCSM3 have the highest liquid water content, greatly exceeding the values observed during the Surface Heat Budget of the Arctic Ocean (SHEBA) campaign. Both GISS-ER and HadCM3 lack liquid water and have excessive ice amounts in Arctic clouds compared to SHEBA observations. In CCSM3, the high surface albedo and strong cloud SW radiative forcing both significantly decrease the amount of SW radiation absorbed by the Arctic Ocean surface during the summer. In the GISS-ER and HadCM3 models, the surface and cloud effects compensate one another: GISS-ER has both a higher summer surface albedo and a larger surface incoming SW flux when compared to HadCM3. Because of the differences in the models' cloud and surface properties, the Arctic Ocean surface gains about 20% and 40% more solar energy during the melt period in the GISS-ER and HadCM3 models, respectively, compared to CCSM3.

In twenty-first-century climate runs, discrepancies in the surface net SW flux partly explain the range in the models' sea ice area changes. Substantial decrease in sea ice area simulated during the twenty-first century in CCSM3 is associated with a large drop in surface albedo that is only partly compensated by increased cloud SW forcing. In this model, an initially high cloud liquid water content reduces the effect of the increase in cloud fraction and cloud liquid water on the cloud optical thickness, limiting the ability of clouds to compensate for the large surface albedo decrease. In HadCM3 and GISS-ER, the compensation of the surface albedo and cloud SW forcing results in negligible changes in the net SW flux and is one of the factors explaining moderate future sea ice area trends. Thus, model representations of cloud properties for today's climate determine the ability of clouds to compensate for the effect of surface albedo decrease on the future shortwave radiative budget of the Arctic Ocean and, as a consequence, the sea ice mass balance.

---

* Lamont-Doherty Earth Observatory Contribution Number 7120.

+ Current affiliation: Laboratoire de Glaciologie et Géophysique de l'Environment, CNRS, Université Joseph Fourier, Grenoble, France.

Corresponding author address: I. V. Gorodetskaya, LGGE, CNRS/UJF-Grenoble, 54 rue Molière, Domaine Universitaire, B.P. 96, 38402 Saint-Martin d'Hères CEDEX, France.
E-mail: irina.gorodetskaya@lgge.obs.ujf-grenoble.fr

DOI: 10.1175/2007JCLI1614.1

1. Introduction

In the summer of 2005, the Arctic sea ice cover decreased to what was probably its smallest extent in at least a century, thus continuing a trend toward less summer ice (Overpeck et al. 2005; Stroeve et al. 2005). As the ice melts, the highly reflective surface is replaced by open water, which absorbs more solar radiation, causing further ice retreat (Curry et al. 1995). This ice–albedo feedback is one of the major factors accelerating melting of the Arctic sea ice in response to the observed increase in the globally averaged temperature (Holland and Bitz 2003). Early climate sensitivity modeling studies (Budyko 1969; Sellers 1969) showed that ice–albedo feedback can strongly amplify initial small perturbations in radiative forcing, leading the climate system to a new stable state, such as entirely ice-covered (decreased forcing) or ice-free ocean (increased forcing). More recently, general circulation models (GCMs) have been used to simulate complicated feedbacks between atmosphere, ocean, land, and sea ice components. Modern GCMs have much lower sensitivity to small changes in radiative forcing compared to simple energy balance models (Houghton et al. 2001). Nevertheless, some GCMs show that the Arctic will lose its perennial ice cover by the time of atmospheric CO_2 doubling, which could occur during this century (Holland et al. 2006; Johannessen et al. 2004; Zhang and Walsh 2006).

Recent modeling studies using GCMs have examined the ice–albedo feedback in the context of other feedbacks and forcings that affect Arctic warming amplification. Hall (2004) found that surface albedo feedback directly accounts only for part of the polar amplification, while it has a significant indirect effect on surface air temperature by increasing summer melt, thus reducing the annual mean sea ice thickness and contributing to the winter atmospheric warming. Winton (2006) showed that the shortwave (SW) feedbacks due to clouds and water vapor inhibit Arctic warming amplification, while surface albedo feedback and cloud-induced longwave feedback favor it. Vavrus (2004) found that differences in cloud feedback between high and low latitudes have a substantial contribution to the polar amplification, in combination with strongly positive snow and sea ice–albedo feedbacks.

In reality, changes in the surface SW radiation budget due to the ice–albedo feedback are inextricably linked to cloud effects (Curry et al. 1996, 1993; Randall et al. 1994; Vavrus 2004). Atmospheric transmittance and solar elevation determine the amount of radiation reaching the surface, part of which is absorbed by the surface, depending on surface albedo. Atmospheric transmittance in turn strongly depends on the cloud water path and the cloud phase. Water droplets are more effective in reflecting and absorbing solar radiation than nonspherical, typically larger ice crystals (Dong et al. 2001). During the Surface Heat Budget of the Arctic Ocean (SHEBA) experiment, a year-long program in the Beaufort Sea, it was found that liquid-dominant mixed-phase clouds at SHEBA were very frequent throughout the year and occurred at temperatures as low as $-25°$ (Intrieri et al. 2002; Shupe et al. 2006). Cloud scenes containing liquid water strongly dominated the SW cloud effect in all sunlit seasons, while ice-only cloud scenes had very little SW shading effect (Shupe and Intrieri 2004; Zuidema et al. 2005). Although the SHEBA conditions cannot be considered as the only "truth" due to high spatial and interannual variability of cloud properties, the averaged mixed-phase microphysical properties observed during SHEBA are within a reasonable range of past in situ observations (Shupe et al. 2006).

Using satellite data of the 1982–98 period in the area north of 60°N, Wang and Key (2003) found a significant negative trend in the surface albedo in the Arctic during the spring and summer. The authors claim that the expected enhancement of the surface net radiation imbalance was reduced or even cancelled out by a concurrent increase in cloud amount, as well as more frequent occurrence of liquid phase clouds. Although the significance of the summer cloud amount trend is disputable due to its small magnitude and short time period, the cloud amount trends in spring are significant, especially over ocean areas (Schweiger 2004). The end of spring and summer surface radiation budget determines the rate of sea ice melt. Thus misrepresentation of cloud properties (including both the cloud amount and cloud particle phase) in models will result in an erroneous estimate of surface net radiation balance and therefore an incorrect sea ice mass budget.

What is the relative role of clouds and surface conditions in controlling the SW radiation budget of the Arctic Ocean? On a seasonal basis, the increase in cloudiness during the summer sea ice melt significantly reduces the effect of the decreased sea ice concentrations (SICs) on the top-of-atmosphere (TOA) albedo (Gorodetskaya et al. 2006). The present study investigates the differences in the net surface SW radiation fluxes attributed to the cloud ice–liquid water content, cloud amounts, sea ice concentrations, and surface albedo in coupled models. We have chosen three coupled GCMs participating in the Intergovernmental Panel on Climate Change (IPCC) Fourth Assessment Report (AR4) that differ significantly in their simulation of

TABLE 1. Description of the coupled climate models used in this study. For the atmospheric components, we list the resolution and number of layers. For the sea ice components, we give the resolution and physics (the summary as in Zhang and Walsh 2006). The last column shows the temperature range when mixed-phase clouds are allowed to form over the ocean or sea ice.

Model	Atmosphere	Sea ice	Mixed-phase clouds
GISS-ER	4° × 5°	4° × 5°	
	20	Energy balance	−4° to −40°C
		Viscous–plastic rheology	
UKMO HadCM3	2.5° × 3.75°	1.25° × 1.25°	
	19	Energy balance	0° to −9°C
		Drifting by ocean currents	
NCAR CCSM3	1.41° × 1.41°	g × lv3(~l°)	
	26	Energy balance	−10° to −40°C
		Thickness distribution	
		Elastic–viscous–plastic rheology	

Arctic cloud and sea ice properties to show how these differences affect the SW radiative balance of the Arctic Ocean. The models are the Goddard Institute for Space Studies Model E-R (GISS-ER), the Met Office Third Hadley Centre Coupled Ocean–Atmosphere GCM (UKMO HadCM3), and the National Center for Atmospheric Research Community Climate System Model, version 3 (NCAR CCSM3). These models have been used intensively for research focusing on Arctic climate (e.g., Bitz et al. 2006; Hansen and Nazarenko 2004; Gregory et al. 2002). At the same time, these models show substantial disagreements in the sea ice area and thickness variations both on a seasonal basis and in twenty-first-century trends (e.g., Arzel et al. 2006). If the models disagree on the net SW radiation budget in the Arctic Ocean in the modern climate, this can lead to errors in the future predictions because of the important role the ice–albedo feedback plays in Arctic warming amplification. A goal of this study is to illustrate disagreements among selected models in the key variables controlling the SW radiation budget. We do not attempt to describe the average performance of all models participating in the IPCC AR4; rather the aim is to provide a case study for such comparisons. Observations, where available, are compared to the model output.

The present study is structured as follows: Section 2 introduces the model and observational data. Results are given in section 3 divided into the following sections: 3a, cloud properties and cloud SW radiative forcing; 3b, sea ice, surface albedo, and clear-sky net surface SW flux; 3c, the combined effects of clouds and surface on the net SW radiation balance at the surface; and 3d, the contribution of the surface and clouds to the net SW flux changes during the twenty-first century. Section 4 gives a summary of the results and conclusions.

2. Model and observational data and methodology

The selected models consider the atmosphere, ocean, sea ice, and land surface components coupled together without flux adjustments. All atmospheric GCMs use a plane-parallel approximation of within-cloud radiative transfer, based on a mean cloud fraction and optical depth. All models include separate treatment of the cloud liquid and cloud ice condensate. Mixed-phase clouds are represented by either the fraction of ice and liquid water prescribed within certain temperature ranges (CCSM3 and HadCM3) or by estimating probabilities of a cloud being all liquid or all ice in a given grid box and at a given time step (GISS-ER). Below we describe the models' simulations and observational data of clouds and sea ice. General information about the models is summarized in Table 1 together with temperature ranges used in each model to define mixed-phase clouds.

In our study we define the Arctic as the ocean area north of 70°N. The twentieth-century analysis is based on 40 model years from January 1959 to December 1998, a period with relatively good observational coverage, though only the SIC data are available during the entire period. The twenty-first-century analysis is based on the two 10-yr periods, January 2000–December 2009 and January 2090–December 2099, referred to as the 2000–10 and 2090–2100 periods. We calculate Arctic mean values using the original model resolutions (see Table 1). For the analysis of relationships among various parameters, the resolutions of atmospheric and sea ice data were adjusted to a common grid. The HadCM3 sea ice data are interpolated onto the atmospheric model grid of 2.5° × 3.75°. In CCSM3, both atmospheric and sea ice data are interpolated onto the 2.5° × 2.5° Earth Radiation Budget Experiment (ERBE) grid. GISS-ER has the same resolution in the atmosphere and sea ice models (4° × 5°).

a. GISS-ER model

A full description of the GISS-ER model can be found in Schmidt et al. (2006). Stratiform cloud water is treated prognostically, with cloud formation based on the available moisture convergence. The phase of cloud water in a given grid box is a function of temperature. The probability of ice condensate increases when the layer temperature decreases from −4° (ocean or sea ice) or −10° (land) to −40°C. The clouds are all ice below −40°C and all liquid above −4°C (−10°C) over oceans (land). After the decision of phase is made, a correction for glaciation of supercooled water droplets (according to the Bergeron–Findeisen "seeder-feeder" process) is applied (Del Genio et al. 1996).

The sea ice model includes a sophisticated thermodynamic scheme and dynamics based on an updated version of Hibler viscous–plastic rheology (Schmidt et al. 2006; Zhang and Rothrock 2000). Albedo parameterization follows Ebert and Curry (1993) and Schramm et al. (1997), including snow "aging" and wetness and spectrally dependent sea ice albedo as a function of ice thickness and parameterized melt pond extent. The ocean component of the Model E-R version is described in Russell et al. (1995).

b. UKMO HadCM3 model

The HadCM3 model is described by Gordon et al. (2000) and Pope et al. (2000). Cloud fraction and cloud condensate are prognostic variables based on a distribution of total water content within a grid box and a critical relative humidity (Gregory and Morris 1996). The model's background aerosol climatology contributes to the outgoing shortwave flux (Cusack et al. 1998). In this model, mixed phase clouds are present between 0° and −9°C (Gordon et al. 2000; Gregory and Morris 1996). Below −9° the cloud condensate in the model exists only as ice crystals. The aircraft measurements, on which the parameterization is based, were obtained in the midlatitude frontal clouds in the eastern part of the North Atlantic and were limited to particles larger than 25 μm (Moss and Johnson 1994). According to Naud et al. (2006), glaciation occurs at very warm temperatures in the clouds typical of frontal ascent regions. Thus, the model parameterization based on the frontal cloud observations underestimates the amount of supercooled liquid water droplets that exists at lower cloud-top temperatures in shallower clouds outside frontal regions.

The sea ice model of HadCM3 uses a simple thermodynamic scheme based on the zero-layer model of Semtner (1976) and sea ice advection by surface ocean current (Cattle and Crossley 1995). The surface albedo is defined as a function of air temperature (equal to 0.8 at −10°C and below, decreasing linearly to 0.5 between −10° and 0°C).

c. NCAR CCSM3 model

The CCSM3 model is described by Collins et al. (2006). Cloud amount is diagnosed by the relative humidity, atmospheric stability, and convective mass fluxes (Boville et al. 2006). Cloud ice and liquid phase condensates are predicted separately (Rasch and Kristjánsson 1998; Zhang et al. 2003), which link the radiative properties of the clouds with their formation and dissipation. Cloud liquid and ice are assumed to coexist within a temperature range of −10° and −40°C (Boville et al. 2006). The clouds are all liquid above −10°C and all ice below −40°C. The radiation budgets generally agree with in situ observations in the polar regions (Briegleb and Bromwich 1998). However, compared with observations, the model produces too much atmospheric moisture in the polar regions and too little in the tropics and subtropics, suggesting that the poleward moisture flux is excessive (Collins et al. 2006).

The sea ice in the CCSM3 is represented by a dynamic–thermodynamic model that includes a subgrid-scale ice thickness distribution, energy conserving thermodynamics, and elastic–viscous–plastic dynamics (Briegleb et al. 2004). The surface albedo for the visible and near-infrared bands is a function of ice and snow thickness and surface temperature.

d. Observational data

SIC data are from the Met Office Hadley Centre's Sea Ice and Sea Surface Temperature (HadISST1) dataset available from 1870 to the present on a 1° latitude–longitude grid (Rayner et al. 2003). Beginning in 1978, the data are derived from the Special Sensor Microwave Imager (SSM/I) and the Scanning Multichannel Microwave Radiometer (SMMR; Gloersen et al. 1992). The microwave radiance data have a monthly averaged SIC error of about 7%, increasing up to 11% during the melt season (Gloersen et al. 1992). The biases are greatly reduced in the HadISST1 homogenization process using other satellite and in situ sea ice concentration and sea ice extent data (Rayner et al. 2003).

The cloud fraction data over the Arctic Ocean are available from the Television and Infrared Observation Satellite (TIROS-N) Operational Vertical Sounder (TOVS) dataset (Francis 1994; Schweiger et al. 1999). This dataset covers the area north of 60°N on an equal area grid with 100-km resolution and is available from July 1979 until December 2001. Over sea ice, TOVS

data were corrected using visible and infrared images from Advanced Very High Resolution Radiometer (AVHRR) and Operational Linescan System and surface observations (Francis 1994). Sea ice cannot be distinguished from clouds that contain a large amount of frozen precipitation. Hence, open-water areas are sometimes interpreted as sea ice (Francis 1994).

The global cloud liquid water path data over the ocean are available from the National Aeronautics and Space Administration (NASA) Water Vapor Project (NVAP) dataset from January 1988 to December 1999 (Randel et al. 1996). The data are derived from SSM/I radiances, while sea ice detection routines were used to remove the high bias in cloud liquid water over the sea ice and polar coastal areas (Cavalieri et al. 1991; Grody 1991). Thus, the data are available only over the ocean areas.

We also use cloud data from the ground-based observations obtained during the SHEBA program in the Beaufort Sea from 20 October 1997 until 1 October 1998 (Intrieri et al. 2002). The details of cloud microphysical retrievals for all-ice and all-liquid clouds are given by Shupe et al. (2005) and for mixed-phase clouds by Shupe et al. (2006). The monthly means of the cloud liquid and ice water paths (IWPs) are calculated from the original data of 1-min resolution provided by M. Shupe. Liquid water paths are derived from the microwave radiometer brightness temperatures at 31.4-GHz frequency (the "liquid" channel insensitive to water vapor or ice), yielding retrievals with 25 g m^{-2} accuracy (Han and Westwater 1995; Westwater et al. 2001). The data are available from 6 December 1997 until 9 September 1998. Cloud ice contents are derived from the vertically pointing 35-GHz cloud radar measurements with an uncertainty of 62%–100% (Shupe et al. 2005). The errors are expected to be smaller for vertically integrated estimates of the ice water path (M. Shupe 2007, personal communication). The IWP data are available from 22 October 1997 to 1 October 1998.

3. Results

a. Cloud properties and surface shortwave cloud forcing

This section focuses on Arctic cloud properties, in particular the cloud fraction and the cloud ice/liquid water content, and their role in reducing the SW flux reaching the surface of the Arctic Ocean. We calculate the SW cloud forcing (SCF) with respect to the incoming radiation at the surface. Thus,

$$\mathrm{SCF} = Q(\mathrm{all}) - Q(\mathrm{clear}),$$

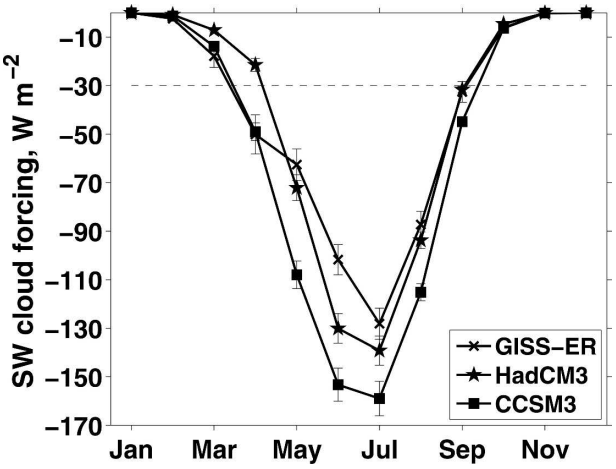

FIG. 1. Surface SCF (the difference between all-sky and clear-sky surface incoming shortwave flux) for the GISS-ER, HadCM3, and CCSM3 models IPCC AR4 twentieth-century simulations. Seasonal cycle for the 1959–98 time period, averaged over the ocean north of 70°N. The error bars are std dev based on monthly means. The dashed line shows the smallest in magnitude SCF during the Arctic melt period (May–September) equal to the GISS-ER and HadCM3 models' September value of 30 W m^{-2}.

where Q(all) and Q(clear) are the amounts of incoming SW radiation at the surface for all-sky conditions and for clear skies only, respectively (Ramanathan et al. 1989; Vavrus 2004). In this case, the cloud SW radiative forcing depends solely on the cloud transmittance.

Figure 1 shows the seasonal cycle of the Arctic mean surface SW cloud forcing in the models. Clouds significantly reduce the incoming SW flux reaching the surface during the Arctic sea ice melt season (May–September), when the solar radiation plays a substantial role in the surface heating and hence the ice melting. During this period CCSM3 has the largest SCF (in magnitude). The difference is especially noticeable in June, when the amount of solar radiation at the TOA over the Arctic Ocean is at its annual maximum (about 500 W m^{-2}). During this month, the GISS-ER Arctic clouds absorb and reflect 60 W m^{-2} less radiation than the CCSM3 clouds and 30 W m^{-2} less than the HadCM3 clouds. We will focus on the summer period to show how different Arctic cloud representations affect the cloud SW forcing.

The HadCM3 and CCSM3 models demonstrate a pronounced seasonal cycle in the cloud fraction with a maximum during summer months (Fig. 2). The cloud fraction in the beginning of the melt period (April–May) and during the sea ice area minimum (September) is noticeably lower in HadCM3. GISS-ER has a large cloud fraction throughout the year. Although the differences in the seasonal cycle are substantial, the

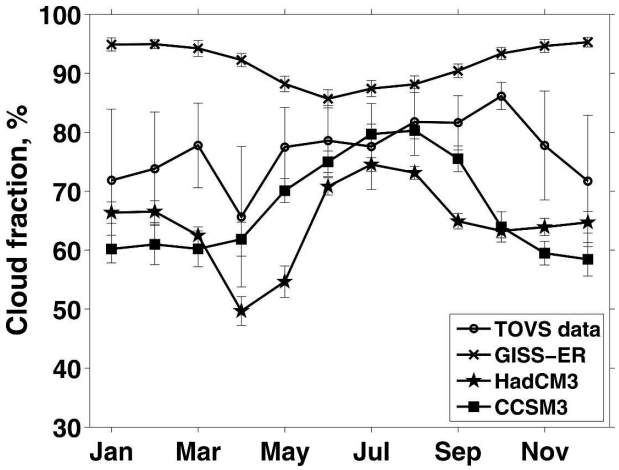

FIG. 2. Total cloud cover fraction averaged over the ocean north of 70°N for the GISS-ER, HadCM3, and CCSM3 models IPCC AR4 twentieth-century simulations and satellite data (TOVS). The model results are for 1959–98. The TOVS data are for 1980–2001. The error bars are std dev based on monthly means.

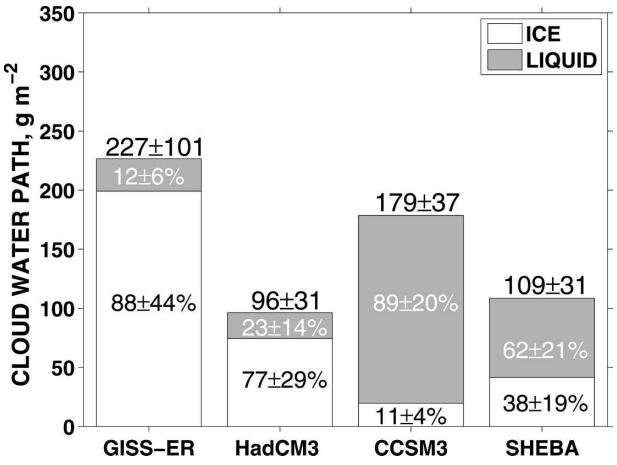

FIG. 3. May–September cloud ice and liquid water paths averaged over the grid boxes closest to the SHEBA locations for the GISS-ER, HadCM3, and CCSM3 models IPCC AR4 twentieth-century simulations and ground-based observations (SHEBA). The numbers above each bar indicate the total cloud water paths (g m^{-2}). The percentages show the partitioning into liquid phase and ice phase. The error estimates are std dev based on monthly means. Model data are averaged over the period from 1959 to 1998. SHEBA data are from 1998.

models all demonstrate high cloudiness in summer in agreement with observations. The average cloud fraction in June–August is 87%, 80%, 73%, and 79% in the GISS-ER, CCSM3, and HadCM3 models and the TOVS data, respectively. Thus, the cloud fraction cannot explain the models' discrepancies in the surface SW cloud forcing (Fig. 1). On the contrary, the model with the highest cloud fraction (GISS-ER) has the smallest summer SW cloud forcing.

More important than the cloud fraction for the surface cloud radiative forcing is the cloud phase, especially during the Arctic melt period. Figure 3 compares the models' LWP and IWP to the SHEBA observations. The relative and absolute magnitudes of the liquid and ice water paths derived for the grid boxes closest to the SHEBA sites are similar to those averaged over the Arctic Ocean in each model. Only the HadCM3 has a mean total cloud water path similar to that of SHEBA's, while the CCSM3 and GISS-ER models have much larger values (Fig. 3). The SHEBA data show a higher proportion of liquid (62%) than ice in the observed clouds (May–September average). The models disagree with the liquid-to-ice cloud proportion, which can be generally characterized by three distinctive cloud water path patterns: 1) small amounts of liquid water and extremely high ice amounts (GISS-ER); 2) small amounts of liquid water and moderate amounts of ice (HadCM3); and 3) large amounts of liquid water and small amounts of ice (CCSM3).

The seasonal cycles of the models' ice and liquid water paths in the Arctic clouds are shown in Fig. 4. We compare the Arctic mean LWP in the models to the NVAP dataset averaged only over the open ocean north of 70°N [due to the large biases in the observations over the ice surface (see section 2)]. The NVAP data show almost constant LWP values around 80 ± 20 kg m^{-2} throughout the year. LWP follows a strong seasonal cycle in all models. The CCSM3 summer LWPs greatly exceed the NVAP data. The HadCM3 and GISS-ER models have no liquid water in their clouds between October and April, while in CCSM3 the liquid phase dominates the cloud water path even during the winter.

The seasonality of the modeled ice and liquid water paths for the grid boxes collocated with the SHEBA experiment (Fig. 5) resembles that of the whole Arctic (Fig. 4). The SHEBA data show large standard deviations based on the daily means. Still, the SHEBA standard deviations are smaller than the differences in the model monthly-mean values of both LWP and IWP. CCSM3 output has significantly higher LWP compared to SHEBA (Fig. 5a). The HadCM3 and GISS-ER models underestimate the LWP during almost the entire year, especially during the nonsummer months. While the clouds of these models contain no liquid water from September through May, the SHEBA mean LWP during January–May is 22 g m^{-2}. The SHEBA LWP data are unavailable for October–November, but the lidar measurements indicate that in November about 45% of clouds contained liquid water (Intrieri et al. 2002). The SHEBA data allow us to compare the models'

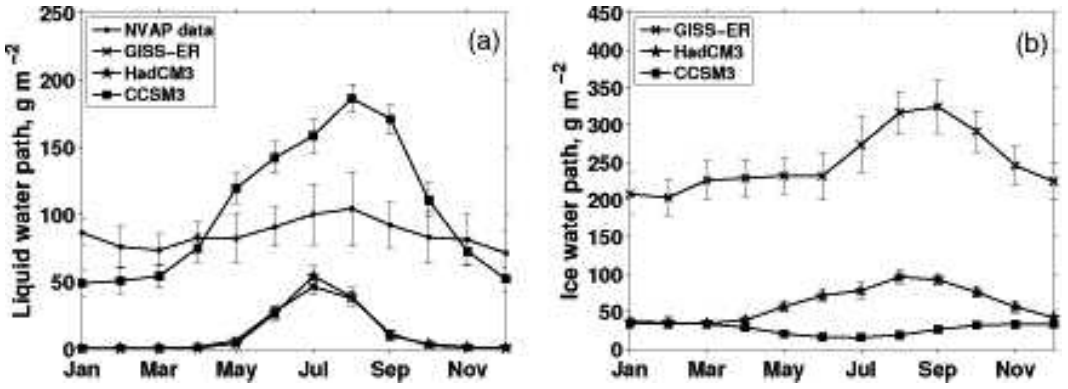

FIG. 4. Cloud (a) liquid water path and (b) ice water path seasonal cycles averaged over the ocean north of 70°N for the GISS-ER, HadCM3, and CCSM3 models IPCC AR4 twentieth-century simulations and liquid water path satellite data (NVAP). Model results are calculated for the 40-yr time period (1959–98). NVAP results are based on the 1988–99 period and include only the ice-free ocean. The error bars are std dev based on monthly means.

IWP to the observed values (Fig. 5b). The HadCM3 and CCSM3 models agree with the relatively low IWP values found during the SHEBA experiment, while GISS-ER significantly overestimates the IWP for the SHEBA locations as well as the Arctic average (Fig. 4b).

In summary, the dominance of the ice phase in GISS-ER Arctic clouds results in much smaller surface SW cloud radiative forcing compared to the other two models, despite the fact that the cloud fraction is the highest in GISS-ER. CCSM3, which has a very large cloud liquid water path, shows the strongest negative SW cloud radiative forcing throughout the sunlit part of the year. Compared to GISS-ER, HadCM3 has a similar cloud liquid water path, but much smaller amounts of cloud ice, and generally smaller cloud fraction. However, the SW surface cloud forcing in this model is stronger during the summer months than in GISS-ER. This may be caused by stronger absorption or reflection within the HadCM3 clouds due to different cloud droplet size parameterization.

b. Sea ice, surface albedo, and clear-sky surface shortwave radiation

The presence of highly reflective ice plays a dominant role in defining the Arctic Ocean surface albedo. Both the sea ice concentrations and the ice properties controlling the albedo of the sea ice (such as ice thickness, snow presence and snow properties, melt ponds, etc.) vary among the models. To summarize their effects on sea ice albedo, we calculated the area-weighted average of the surface albedo for each 10% SIC bin

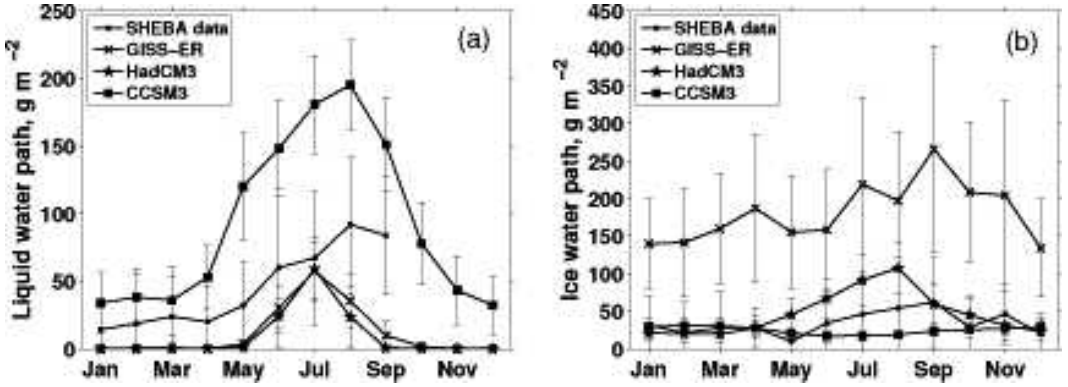

FIG. 5. Cloud (a) liquid water path and (b) ice water path seasonal cycles averaged over the grid boxes closest to the SHEBA sites for the GISS-ER, HadCM3, and CCSM3 models IPCC AR4 twentieth-century simulations and ground-based observations (SHEBA). Model data are averaged over the period from 1959 to 1998. SHEBA data are from October 1997 to September 1998. The error bars are std dev based on daily means for SHEBA and on monthly means for models.

averaged over the entire 40-yr time period during sunlit months for grid boxes where sea ice appears (Fig. 6). The radiative effectiveness (RE) of sea ice with respect to the surface albedo, defined as a difference between the albedo over 100% and 0% SIC, is 0.53, 0.60, and 0.66 for GISS-ER, CCSM3, and HadCM3, respectively. GISS-ER has the lowest RE due to the low sea ice albedo. The other two models agree on the sea ice albedo for 90%–100% SIC. CCSM3 has a higher open ocean surface albedo, which influences the low SIC bins. In CCSM3 and HadCM3, the major factor causing variations in the surface albedo of the Arctic Ocean is the sea ice concentration, while in GISS-ER the effect of sea ice properties is more important.

The Arctic sea ice area and mean surface albedo are shown in Fig. 7. All models show larger sea ice areas compared to the satellite data in the winter (Fig. 7a). In the summer, the sea ice area is significantly overestimated in GISS-ER, slightly underestimated in HadCM3, and close to the observed in CCSM3. The small summer sea ice area reduces the surface albedo in HadCM3 (Fig. 7b). A significant amount of open water is simulated during the melt period in HadCM3, the largest among the models. At the same time, the ice pack in GISS-ER is characterized by high SICs even during the summer melt period, while the Arctic mean surface albedo is similar to CCSM3. Maps of sea ice concentrations, surface albedo, and clear-sky surface net SW radiation averaged during June–August (Fig. 8) show that CCSM3 has a high albedo over central Arctic perennial ice (0.5–0.6) together with lower than 80% SIC in peripheral seas, while in GISS-ER the entire Arctic is locked in ice (>90% SICs) with relatively low ice albedo (0.3–0.5). This gives comparable Arctic mean surface albedo in the two models (Fig. 7b) and thus the clear-sky net SW flux at the surface (Figs. 8a,c). Much smaller surface albedo and thus larger clear-sky net SW radiation flux at the surface in HadCM3 compared to the other two models is caused by the higher percentage of open water within the pack ice (lower SICs) in HadCM3 (Fig. 8b).

c. *Combined cloud and sea ice effects on surface net shortwave flux*

The amount of solar radiation gained by the surface is a function of both the cloud radiative forcing and the surface albedo. Until now, we have discussed separately the sea ice and cloud effects on the incoming or clear-sky net SW radiation. This section presents their combined effects on the net SW flux at the surface, which represents the solar energy gained by the Arctic Ocean.

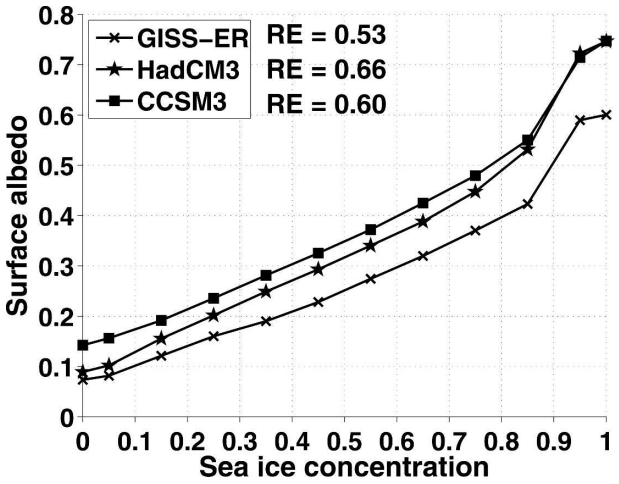

FIG. 6. Area-weighted mean surface albedo as a function of sea ice concentrations for the GISS-ER, HadCM3, and CCSM3 models IPCC AR4 twentieth-century simulations. Based on monthly mean data (1959–98) during sunlit months over the grid boxes where sea ice appears at least during one month over the 40-yr period in each model. RE = albedo (100% ice concentration) − albedo (0% ice concentration).

At the beginning of the melt season, models show very large differences in the surface net SW flux averaged over the Arctic Ocean for all-sky conditions (Fig. 9). The Arctic Ocean gains 25% (27 W m^{-2}) and 40% (44 W m^{-2}) more energy in June in the GISS-ER and HadCM3 models, respectively, compared to CCSM3 (or 19% and 39%, respectively, during the sea ice melt period, May–September, average). For CCSM3 and HadCM3, the difference in surface net SW radiation is due to the cloud and surface reflection, as the models' climatological values for the SW radiation absorbed by the atmosphere agree (Fig. 10). Slightly lower atmospheric absorption in GISS-ER (with maximum difference of 10 W m^{-2} in July compared to the other two models) contributes to the highest net SW flux at the surface in this model.

Figure 11 presents the spatial distribution of the surface SW cloud forcing and all-sky surface net SW radiation averaged during June–August. Comparison of Fig. 11 with Fig. 8 shows how the cloud radiative forcing modulates the surface albedo influence. Optically thick clouds in CCSM3 decrease the net absorbed SW radiation at the surface (Fig. 11c). This exacerbates the effect of the high surface albedo on net SW radiation over the ice-covered Arctic (Fig. 8c). In HadCM3, stronger cloud SW forcing compared to GISS-ER compensates for their differences in surface albedo (Figs. 11a,b and 8a,b). The net SW radiation at the surface agrees in these two models despite the differences in surface and cloud properties.

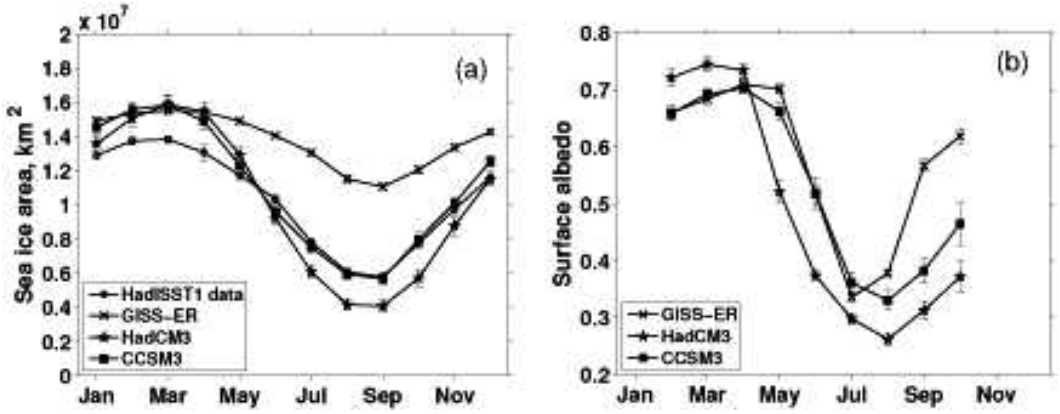

FIG. 7. Seasonal cycles of total Arctic (a) sea ice area and (b) surface albedo averaged over the ocean north of 70°N for the GISS-ER, HadCM3, and CCSM3 models IPCC AR4 twentieth-century simulations and sea ice area satellite data (HadISST1). Sea ice areas are calculated using the ice concentrations and thus account for openings within the pack ice. Both model and satellite data results are for the 1959–98 period. The error bars are std dev based on monthly means.

Surface albedo and cloud SW forcing are the main contributors to the net SW radiation at the surface: variability of these two parameters explains 47%, 79%, and 73% of the net SW radiation variability in the GISS-ER, HadCM3, and CCSM3 models, respectively. The estimate is based on monthly data during the sunlit months, March to September, when the net SW flux at the surface is greater than 10 W m^{-2} (Fig. 9). Table 2 shows correlation coefficients between monthly anomalies of the net SW radiation at the surface and each of the two parameters, surface albedo and SW cloud forcing. The correlations are computed for the entire year ("Total") and separately for each month. This shows the contribution of surface and clouds to the net SW flux interannual variability. Contribution of the covariability of cloud SW forcing and surface albedo to the net SW flux is negligible in all the models and thus is not shown.

Cloud SW forcing dominates variability of the net SW radiation at the surface over the course of the year in HadCM3 (Table 2). In CCSM3 and GISS-ER, surface albedo in total slightly dominates over the cloud effects on the net SW radiation. However, monthly correlations show that the dominating influence on the net SW flux shifts from surface albedo to cloud forcing over the year in all three models. In both GISS-ER and HadCM3, surface albedo variability significantly dominates the net SW flux during all sunlit months, except for July–August in GISS-ER and June–September in HadCM3. During these months the Arctic mean surface albedo drops below 0.4 (Fig. 7b) and has relatively low variability (calculated as the standard deviation based on the Arctic mean monthly values). Such a low Arctic mean albedo is characteristic of the extensive melt in the Arctic. Thus, the larger overall contribution of cloud variability to the net SW radiation in HadCM3 is related to the longer melt season in this model. In CCSM3, although surface albedo variability dominates the net SW flux over the year, cloud forcing variability has a significant influence in all sunlit months, overwhelming the surface signal in July–August (Table 2). High surface albedo variability in CCSM3 increases the contribution of surface albedo to the net SW flux even during July–August. We speculate that this is due to the more variable ice dynamics from year to year in CCSM3 compared to the other two models.

To assess the connection between the interannual variability in the summer net SW flux absorbed by the Arctic Ocean and the sea ice area reduction during the summer, we correlated the summer mean net SW flux (May–August average) averaged over the Arctic Ocean north of 70°N with September sea ice area. The correlation coefficients are −0.6 and −0.4 significant at the 95% level in CCSM3 and HadCM3, respectively. In HadCM3 interannual variability of the summer net SW flux is mostly dominated by variability of the cloud forcing, while in CCSM3 the dominance of the cloud forcing and surface albedo is comparable during the summer (Table 2). In GISS-ER, the interannual variability of the summer net SW flux has a small but negative correlation with the September sea ice area [$r = -0.12$, p value = 0.46 (correlation is not significant)]. The large amount of net SW radiation absorbed by sea ice in GISS-ER is used to reduce the sea ice volume from the very large winter values (results not shown) with a negligible effect on the sea ice area.

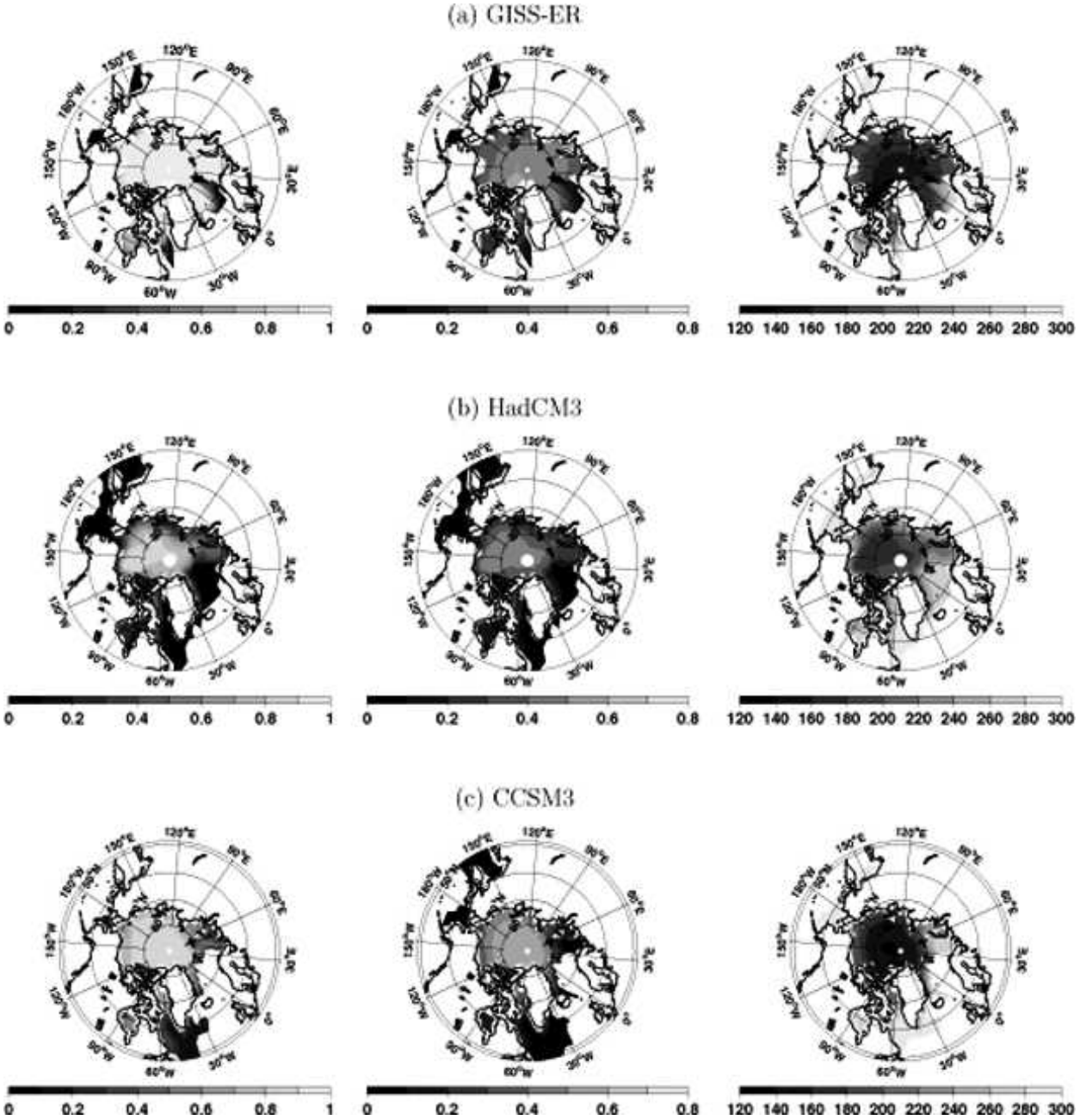

FIG. 8. Maps of spatial distribution of the (left) sea ice concentrations, (center) surface albedo, and (right) clear-sky surface net shortwave flux (W m^{-2}) averaged for June–August, 1959–98, for (a) GISS-ER, (b) HadCM3, and (c) CCSM3 models IPCC AR4 twentieth-century simulations. The data are plotted for the areas of maximum sea ice extent in each model north of 50°N.

d. Surface net shortwave flux in the twenty-first century

The differences in the Arctic sea ice and cloud properties and their effects on the surface SW radiation budget discussed above can partly explain the AR4 models' discrepancies in the future sea ice trends. We compare the seasonal cycles of the Arctic Ocean mean SW fluxes at the surface for the first and last decades of the twenty-first century from the Special Report on Emission Scenarios (SRES) A1B model simulations. The SRES A1B is a "moderate" scenario forcing, where atmospheric CO_2 concentration doubles by 2100 (Houghton et al. 2001).

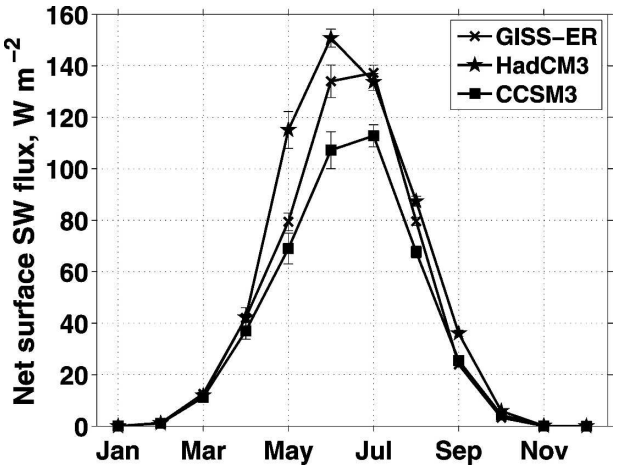

FIG. 9. Seasonal cycle of the all-sky net surface shortwave flux averaged over the ocean north of 70°N for GISS-ER, HadCM3, and CCSM3 models IPCC AR4 twentieth-century simulations for the 1959–98 period. The error bars are std dev based on monthly means.

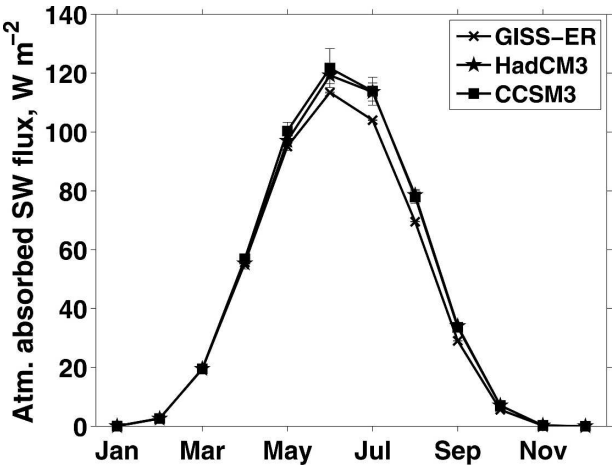

FIG. 10. Seasonal cycle of the all-sky shortwave flux absorbed by the atmosphere averaged over the ocean north of 70°N for GISS-ER, HadCM3, and CCSM3 models IPCC AR4 twentieth-century simulations for the 1959–98 period. The error bars are std dev based on monthly means.

Figure 12 shows the net SW flux seasonal cycle during the 2000–10 and the 2090–2100 periods, as well as the contribution of the cloud and surface albedo changes to the net SW flux difference between the two decades. CCSM3 predicts an increase in the annual mean Arctic cloudiness and cloud liquid water content (results not shown) together with a significant drop in the Arctic mean surface albedo, especially during the melt period, by the end of the twenty-first century. However, the decrease in the surface downwelling SW radiation is not large enough to compensate for the surface albedo decrease, and the net SW flux at the surface increases substantially during the summer with a maximum increment of 24 W m^{-2} in June (Fig. 12c). HadCM3 also predicts a significant drop in the surface albedo, but this is almost entirely compensated by the increased SW cloud forcing, resulting in a very small increase in the net SW flux at the surface during the summer (maximum increment of 6 W m^{-2} in June) (Fig. 12b). In GISS-ER surface albedo decreases significantly during June–July, but is compensated by the large increase in cloud forcing, resulting in practically no change in the net SW flux (Fig. 12a). Thus in HadCM3 and GISS-ER the compensation of the surface albedo and cloud forcing effects reduces the changes in the surface net SW flux in the twenty-first-century climate simulations and could be one of the factors explaining moderate future sea ice volume trends (Arzel et al. 2006). In the CCSM3 case, the cloud forcing changes do not compensate for the surface albedo decrease resulting in a significant increase in the SW flux absorbed by the Arctic Ocean, which may explain the large drop in sea ice area in the twenty-first-century simulations.

4. Summary and conclusions

We have analyzed the effects of sea ice concentrations, surface albedo, cloud cover, and cloud ice/liquid water content on the Arctic shortwave radiation balance in the IPCC AR4 twentieth-century simulations of three coupled models: GISS-ER, the UKMO HadCM3 model, and the NCAR CCSM3 model. The model seasonal cycles and climatology from 1959 to 1998 were compared to the satellite and ground-based observations available during this 40-yr time period. We also showed the contribution of the cloud and surface albedo changes to the difference in the surface net SW flux seasonal cycle between the beginning and the end of the twenty-first century.

The sea ice melt occurring in the Arctic during the summer is largely triggered by the solar radiative heating of the surface. Thus the ability of any model to simulate the summer sea ice melt process strongly depends on the simulation of the net SW radiation budget. Our results based on three coupled models that are intensively used for global and Arctic climate research show that the cloud phase and the surface albedo are the major parameters responsible for the models' differences in the net SW flux at the surface. The Arctic Ocean in HadCM3 receives the largest amount of the solar flux, while in CCSM3 it receives the least (with the maximum difference of 44 W m^{-2} occurring in June). Over the entire sunlit part of the year the net SW flux

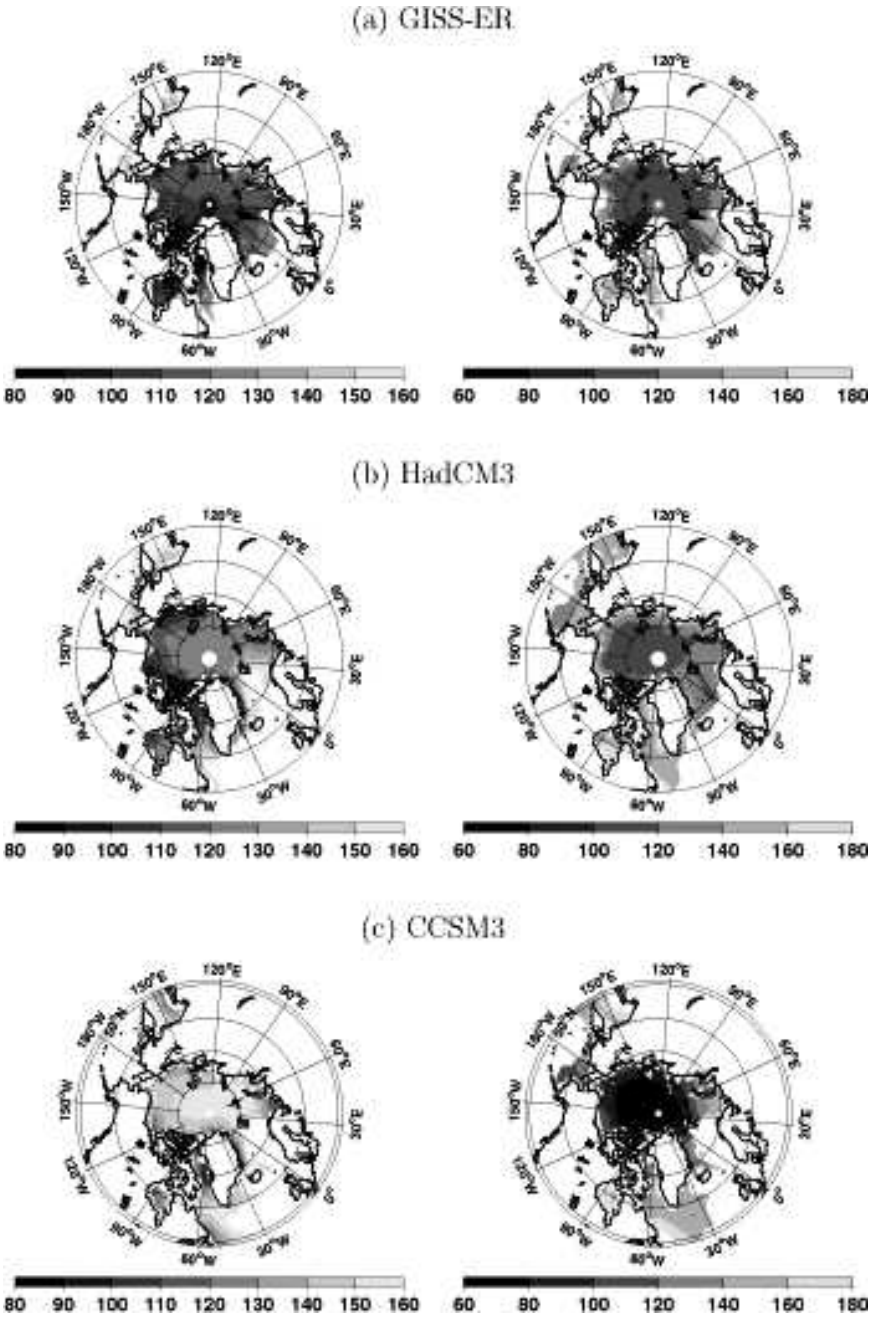

FIG. 11. Maps of spatial distribution of the (left) surface shortwave cloud forcing (W m^{-2}) and (right) all-sky surface net shortwave radiation (W m^{-2}) averaged for June–August, 1959–98, for (a) GISS-ER, (b) HadCM3, and (c) CCSM3 models IPCC AR4 twentieth-century simulations. Cloud forcing is calculated as the difference between incoming shortwave radiation at the surface for clear-sky and for all-sky conditions (positive = cooling). The data are plotted for the area of maximum sea ice extent north of 50°N.

variability has stronger correlation with the surface albedo in the GISS-ER and CCSM3 models and with the cloud forcing in HadCM3. However, the control of the net SW flux switches from cloud forcing to surface albedo over the annual cycle. This shows that both the seasonal variability and the models' differences in the net SW flux are determined by a complex relationship between surface and clouds rather than by a dominant signal of one of them.

Coupled models participating in the IPCC AR4 as-

TABLE 2. Correlation coefficients between the net shortwave radiation at the surface and each of the two parameters: surface albedo (α_s) and SCF for sunlit months, when net shortwave radiation at the surface averaged over the ocean north of 70°N is greater than 10 W m^{-2}. Total estimates also include the variance in the net shortwave flux explained by each parameter (R^2/%). The calculations are based on monthly mean anomalies of the values averaged over the ocean north of 70°N for GISS-ER, HadCM3, and CCSM3 models IPCC AR4 twentieth-century simulations. Bold shows the correlations greater than or equal to 0.5. All correlations are significant at the 95% level, except for those marked with an asterisk (*).

	GISS-ER		HadCM3		CCSM3	
Models	$1 - \alpha_s$	SCF	$1 - \alpha_s$	SCF	$1 - \alpha_s$	SCF
Total	**0.56/31**	0.40/16	0.33/11	**0.65/42**	**0.65/42**	0.5/25
Mar	**0.89**	0.15*	**0.95**	−0.6	**0.59**	**0.62**
Apr	**0.94**	−0.18*	**0.91**	0.11*	**0.62**	**0.56**
May	**0.91**	0.48	**0.77**	0.05*	**0.73**	0.33
Jun	**0.78**	0.42	0.28*	**0.87**	**0.88**	0.44
Jul	0.06*	**0.68**	0.08*	**0.92**	**0.56**	**0.68**
Aug	0.21*	**0.56**	0.08*	**0.90**	0.44	**0.59**
Sep	**0.74**	0.13*	0.29*	**0.67**	**0.58**	**0.50**

sessment show large discrepancies in future Arctic sea ice thickness and extent (e.g., Arzel et al. 2006). The three models considered in this study span almost the entire range of predicted sea ice response: by the end of the twenty-first century the Arctic sea ice extent declines by about 6×10^6 km^2 in CCSM3 (extreme response), 4×10^6 km^2 in HadCM3 (moderate response), and "only" 1×10^6 km^2 in GISS-ER (conservative response). The differences in the Arctic sea ice and cloud properties and their effects on the surface SW radiation budget demonstrated by this study partly explain the AR4 models' range in the future sea ice trends. Below we summarize the results for each model of the combined effects of sea ice and clouds on the net SW radiation at the surface in the twentieth- and twenty-first-century simulations.

The strong cloud shortwave forcing in CCSM3 (with a maximum of 160 W m^{-2} in June) is associated with high cloud liquid water path throughout the year and exacerbates the effect of high sea ice albedo on the net SW radiation at the Arctic Ocean surface. Other heat fluxes, such as longwave cloud forcing, ocean heat transport, and atmospheric heat advection should compensate for the deficiency in the surface SW radiation budget. Despite the relatively small summer net SW flux at the surface, its variability is well correlated with the summer sea ice area reduction. A strong sea ice area decline in the twenty-first century in this model is associated with a significant decrease in surface albedo, which is only partly compensated by the increased cloud cooling. An initially high cloud liquid water content reduces the effect of the increase in cloud fraction and cloud liquid water on the cloud optical thickness. This explains the inability of clouds to compensate for the surface albedo decrease and needs further investigation as does the role of the longwave cloud forcing.

In the HadCM3 and GISS-ER models clouds and surface have the opposite effects on the surface shortwave energy budget: the model with a higher summer surface albedo has a weaker SW cloud forcing (GISS-ER), as compared to the model with a lower surface albedo (HadCM3). This reduces the models' differences in the surface net SW radiation. The compensation of the surface albedo and cloud forcing effects reduces the changes in the surface net SW flux also in the twenty-first-century climate simulations and could be one of the factors explaining moderate future sea ice volume trends in the HadCM3 and GISS-ER models (Arzel et al. 2006).

Large amounts of open water occur within the Arctic ice pack during the summer melt period in HadCM3, leading to the lowest Arctic surface albedo. The low surface albedo effect dominates over the relatively strong cloud radiative forcing effect in determining the largest surface net SW flux during the melt period in this model. This strong summer solar heating of the Arctic Ocean surface is consistent with HadCM3 having the largest reduction in the sea ice area during the summer. At the same time, interannual variability in the summer net SW flux is dominated by variability in the cloud forcing rather than surface albedo.

Despite the high cloud fraction (about 90%) in GISS-ER, the prevalence of ice phase reduces clouds' radiative forcing and allows large amounts of solar radiation to reach the Arctic Ocean surface. High sea ice concentrations, even in summer, compensate for this excessive incoming radiation. They increase the surface albedo in the Arctic peripheral seas, which in reality are ice-free during the summer. However, the effect of excessive summer sea ice concentrations on the surface albedo is mitigated by the lower sea ice albedo in GISS-ER. In this model, sea ice albedo during summer is reduced by extensive melt pond formation, where 30% of the meltwater at the surface is converted to pond volume (G. Schmidt 2007, personal communication). The large amount of SW radiation absorbed by sea ice in GISS-ER is used to reduce the sea ice volume from the very large winter values with a negligible effect on the sea ice area. This explains lack of correlation between the interannual variability of the summer net SW flux at the Arctic Ocean surface and September sea ice area. Interannual variability in the net SW flux itself is controlled by cloud forcing during the short summer

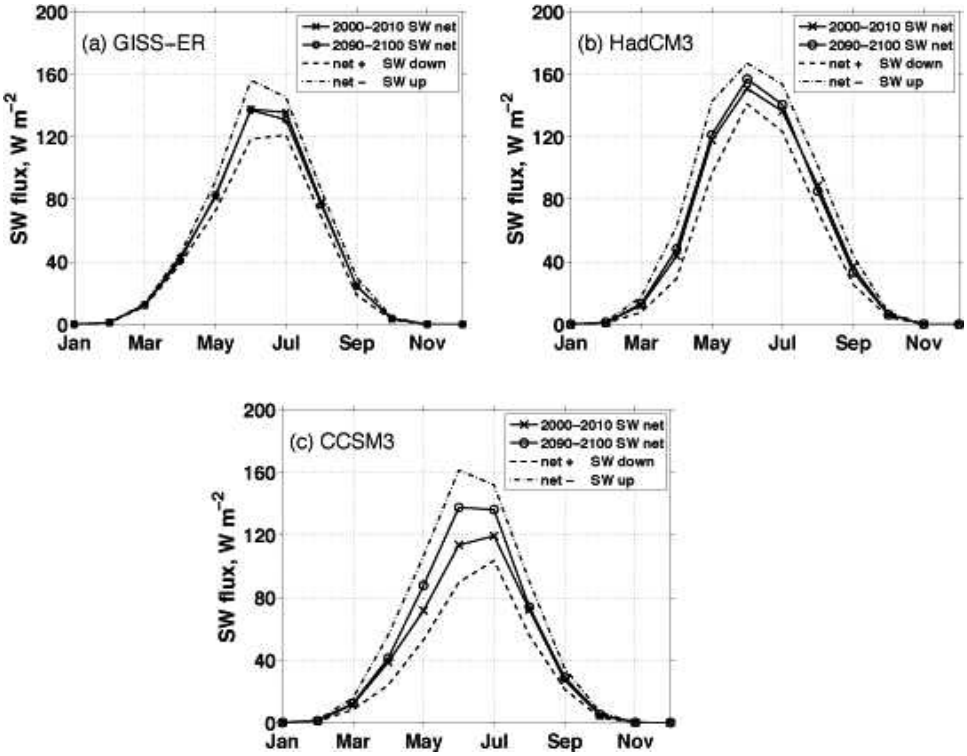

FIG. 12. Seasonal cycle of the all-sky net surface shortwave flux averaged over the ocean north of 70°N for GISS-ER, HadCM3, and CCSM3 models IPCC AR4 twenty-first-century simulations forced with the SRES A1B scenario. The 10-yr monthly means are shown for the 2000–10 and 2090–2100 periods. The "net $+\Delta$SW down" is the atmospheric contribution and the "net $-\Delta$SW up" is the surface albedo contribution to the difference between the net SW flux for two periods.

melt (July–August) and predominantly by surface albedo during other sunlit months.

The changes in the Arctic climate will be manifested in changes of both surface and cloud properties. There is a large uncertainty in the possible climate system response due to the poor understanding of the Arctic cloud microphysical characteristics. The predicted substantial decrease in Arctic summer sea ice concentrations during the twenty-first century may favor cloud formation, which should diminish or even cancel the ice–albedo feedback by shielding the surface (Kato et al. 2006). However, an expected increase in storm activity and cyclogenesis in the Arctic (McCabe et al. 2001) has the potential to increase the ice fraction in the Arctic clouds (Naud et al. 2006). This will decrease the cloud shortwave radiative forcing, making them more "transparent" and allowing sea ice changes to have a greater influence on the surface radiative balance. If clouds are already characterized by high cloud optical thickness, as in the CCSM3 model, its future increase will have only a small impact on the shortwave flux. In both scenarios, the decrease in the surface albedo will not be compensated by increased cloud shortwave forcing and thus will dominate the increase in the shortwave radiation absorbed by the Arctic Ocean, accelerating the sea ice decline. Another scenario is when a significant reduction in surface albedo during the melt period is almost entirely compensated by the increased shortwave cloud forcing, as found in the twenty-first-century simulations in HadCM3 and GISS-ER. This diminishes the importance of the ice–albedo feedback in the sea ice area decline. The decline in the Arctic sea ice causes Arctic Ocean mean surface albedo to decrease triggering the ice–albedo feedback. The ability of clouds to compensate for this strong positive feedback during the twenty-first century depends on model representations of cloud properties for today's climate with important consequences for future sea ice mass balance.

Acknowledgments. We thank Anthony Del Genio for help in understanding cloud treatment in GCMs, in particular in the GISS Model E; Steve Vavrus for discussing cloud parameterization in CCSM3; Gavin Schmidt

for information about GISS-ER sea ice; Paquita Zuidema for valuable discussions and encouragement; and Steve Warren, Tom Grenfell, and Axel Schweiger for their feedbacks. We are grateful to Matthew Shupe for providing SHEBA data together with information about their accuracy and discussing the results. Our great appreciation to all the people involved in the SHEBA field work and subsequent data processing. We acknowledge the international modeling groups for providing their data for analysis, the Program for Climate Model Diagnosis and Intercomparison (PCMDI) for collecting and archiving the model data, the JSC/CLIVAR Working Group on Coupled Modelling (WGCM) and their Coupled Model Intercomparison Project (CMIP) and Climate Simulation Panel for organizing the model data analysis activity, and the IPCC WG1 TSU for technical support. The IPCC Data Archive at Lawrence Livermore National Laboratory is supported by the Office of Science, U.S. Department of Energy. We thank the National Snow and Ice Data Center, the Hadley Center for Climate Prediction and Research, the NVAP team, and the TOVS team for providing satellite data. We appreciate the efforts of the two anonymous reviewers for their positive feedback and constructive criticism, which helped to significantly improve the manuscript. Gorodetskaya was supported by NASA Fellowship ESSF0400000163; Tremblay was supported by NSF Grants OPP-0230264 and OPP-0230325 and jointly with Cullather by Grant ARC-05-20496; Liepert was supported by NSF Climate Dynamics Program Contract ATM02-24807; Cane was supported by CORC ARCHES, NOAA. This research was funded in part under the Cooperative Institute for Climate Applications and Research (CICAR) Award NA03OAR4320179 from NOAA, U.S. Department of Commerce.

REFERENCES

Arzel, O., T. Fichefet, and H. Goosse, 2006: Sea ice evolution over the 20th and 21st centuries as simulated by current AOGCMs. *Ocean Modell.,* **12,** 401–415.

Bitz, C. M., P. R. Gent, R. A. Woodgate, M. M. Holland, and R. Lindsay, 2006: The influence of sea ice on ocean heat uptake in response to increasing CO_2. *J. Climate,* **19,** 2437–2450.

Boville, B. A., P. J. Rasch, J. J. Hack, and J. R. McCaa, 2006: Representation of clouds and precipitation processes in the Community Atmosphere Model Version 3 (CAM3). *J. Climate,* **19,** 2184–2198.

Briegleb, B. P., and D. H. Bromwich, 1998: Polar radiation budgets of the NCAR CCM3. *J. Climate,* **11,** 1246–1269.

——, C. M. Bitz, E. C. Hunke, W. H. Lipscomb, M. M. Holland, J. L. Schramm, and R. E. Moritz, 2004: Scientific description of the sea ice component in the Community Climate System Model, version three. Tech. Rep. NCAR/TN-463+STR, 78 pp.

Budyko, M. I., 1969: The effects of solar radiation on the climate of the earth. *Tellus,* **21,** 611–619.

Cattle, H., and J. Crossley, 1995: Modelling Arctic climate change. *Philos. Trans. Roy. Soc. London,* **A352,** 201–213.

Cavalieri, D. J., J. P. Crawford, M. R. Drinkwater, D. T. Eppler, L. D. Farmer, R. R. Jentz, and C. C. Wackerman, 1991: Aircraft active and passive microwave validation of sea ice concentration from the Defense Meteorological Satellite Program special sensor microwave imager. *J. Geophys. Res.,* **96,** 21 989–22 008.

Collins, W. D., and Coauthors, 2006: The Community Climate System Model version 3 (CCSM3). *J. Climate,* **19,** 2122–2143.

Curry, J. A., J. L. Schramm, and E. E. Ebert, 1993: Impact of clouds on the surface radiation balance of the Arctic Ocean. *Meteor. Atmos. Phys.,* **51,** 197–217.

——, ——, and ——, 1995: Sea ice-albedo climate feedback mechanism. *J. Climate,* **8,** 240–247.

——, W. B. Rossow, D. Randall, and J. L. Schramm, 1996: Overview of Arctic cloud and radiation characteristics. *J. Climate,* **9,** 1731–1764.

Cusack, S., A. Slingo, J. M. Edwards, and M. Wild, 1998: The radiative impact of a simple aerosol climatology on the Hadley Centre atmospheric GCM. *Quart. J. Roy. Meteor. Soc.,* **124,** 2517–2526.

Del Genio, A. D., M.-S. Yao, W. Kovari, and K. K.-W. Lo, 1996: A prognostic cloud water parameterization for global climate models. *J. Climate,* **9,** 270–304.

Dong, X., G. G. Mace, P. Minnis, and D. F. Young, 2001: Arctic stratus cloud properties and their effect on the surface radiation budget: Selected cases from FIRE ACE. *J. Geophys. Res.,* **106,** 15 297–15 312.

Ebert, E. E., and J. A. Curry, 1993: An intermediate one-dimensional thermodynamic sea ice model for investigating ice-atmosphere interactions. *J. Geophys. Res.,* **98,** 10 085–10 109.

Francis, J. A., 1994: Improvements of TOVS retrievals over sea ice and applications to estimating Arctic energy fluxes. *J. Geophys. Res.,* **99,** 10 395–10 408.

Gloersen, P., W. J. Campbell, D. J. Cavalieri, J. C. Comiso, C. L. Parkinson, and H. J. Zwally, 1992: Arctic and Antarctic sea ice, 1978–1987: Satellite passive microwave observations and analysis. NASA SP-511, 290 pp.

Gordon, C., C. Cooper, C. A. Senior, H. Banks, J. M. Gregory, T. C. Johns, J. F. B. Mitchell, and R. Wood, 2000: The simulation of SST, sea ice extents and ocean heat transports in a version of the Hadley Centre coupled model without flux adjustments. *Climate Dyn.,* **16,** 147–168.

Gorodetskaya, I. V., M. A. Cane, L.-B. Tremblay, and A. Kaplan, 2006: The effects of sea ice and land snow concentrations on planetary albedo from the Earth Radiation Budget Experiment. *Atmos.–Ocean,* **44,** 195–205.

Gregory, D., and D. Morris, 1996: The sensitivity of climate simulations to the specification of mixed phase clouds. *Climate Dyn.,* **12,** 641–651.

——, D. Wilson, and A. Bushell, 2002: Insights into cloud param-

etrization provided by a prognostic approach. *Quart. J. Roy. Meteor. Soc.,* **128,** 1485–1504.

Grody, N. C., 1991: Classification of snow cover and precipitation using the Special Sensor Microwave/Imager (SSM/I). *J. Geophys. Res.,* **96,** 7423–7435.

Hall, A., 2004: The role of surface albedo feedback in climate. *J. Climate,* **17,** 1550–1568.

Han, Y., and E. R. Westwater, 1995: Remote sensing of tropospheric water vapor and cloud liquid water by integrated ground-based sensors. *J. Atmos. Oceanic Technol.,* **12,** 1050–1059.

Hansen, J., and L. Nazarenko, 2004: Soot climate forcing via snow and ice albedos. *Proc. Natl. Acad. Sci. USA,* **101,** 423–428.

Holland, M. M., and C. M. Bitz, 2003: Polar amplification of climate change in coupled models. *Climate Dyn.,* **21,** 221–232.

——, ——, and B. Tremblay, 2006: Future abrupt reductions in the summer Arctic sea ice. *Geophys. Res. Lett.,* **33,** L23503, doi:10.1029/2006GL028024.

Houghton, J. T., Y. Ding, D. J. Griggs, M. Noguer, P. J. van der Linden, X. Dai, K. Maskell, and C. A. Johnson, Eds., 2001: *Climate Change 2001: The Scientific Basis.* Cambridge University Press, 881 pp.

Intrieri, J. M., M. D. Shupe, T. Uttal, and B. J. McCarty, 2002: An annual cycle of Arctic cloud characteristics observed by radar and lidar at SHEBA. *J. Geophys. Res.,* **107,** 8030, doi:10.1029/2000JC000423.

Johannessen, O. M., and Coauthors, 2004: Arctic climate change: Observed and modelled temperature and sea-ice variability. *Tellus,* **56A,** 328–341.

Kato, S., N. G. Loeb, P. Minnis, J. A. Francis, T. P. Charlock, D. A. Rutan, E. E. Clothiaux, and S. Sun-Mack, 2006: Seasonal and interannual variations of top-of-atmosphere irradiance and cloud cover over polar regions derived from the CERES data set. *Geophys. Res. Lett.,* **33,** L19804, doi:10.1029/2006GL026685.

McCabe, G. J., M. P. Clark, and M. C. Serreze, 2001: Trends in Northern Hemisphere surface cyclone frequency and intensity. *J. Climate,* **14,** 2763–2768.

Moss, S. J., and D. W. Johnson, 1994: Aircraft measurements to validate and improve numerical model parametrisations of ice to water ratios in clouds. *Atmos. Res.,* **34,** 1–25.

Naud, C. M., A. D. Del Genio, and M. Bauer, 2006: Observational constraints on the cloud thermodynamic phase in midlatitude storms. *J. Climate,* **19,** 5273–5288.

Overpeck, J. T., and Coauthors, 2005: Arctic system on trajectory to new, seasonally ice-free state. *Eos, Trans. Amer. Geophys. Union,* **86,** 309–313.

Pope, V. D., M. L. Gallani, P. R. Rowntree, and R. A. Stratton, 2000: The impact of new physical parametrizations in the Hadley Centre climate model: HadAM3. *Climate Dyn.,* **16,** 123–146.

Ramanathan, V., R. D. Cess, E. F. Harrison, P. Minnis, B. R. Barkstrom, E. Ahmad, and D. Hartmann, 1989: Cloud-radiative forcing and climate: Results for the Earth Radiation Budget Experiment. *Science,* **243,** 57–63.

Randall, D. A., and Coauthors, 1994: Analysis of snow feedbacks in 14 general circulation models. *J. Geophys. Res.,* **99,** 20 757–20 772.

Randel, D. L., T. H. Vonder Haar, M. A. Ringerud, G. L. Stephens, T. J. Greenwald, and C. L. Combs, 1996: A new global water vapor dataset. *Bull. Amer. Meteor. Soc.,* **77,** 1233–1246.

Rasch, P. J., and J. E. Kristjánsson, 1998: A comparison of the CCM3 model climate using diagnosed and predicted condensate parameterizations. *J. Climate,* **11,** 1587–1614.

Rayner, N. A., D. E. Parker, E. B. Horton, C. K. Folland, L. V. Alexander, D. P. Rowell, E. C. Kent, and A. Kaplan, 2003: Global analyses of sea surface temperature, sea ice, and night marine air temperature since the late nineteenth century. *J. Geophys. Res.,* **108,** 4407, doi:10.1029/2002JD002670.

Russell, G. L., J. R. Miller, and D. Rind, 1995: A coupled atmosphere–ocean model for transient climate change studies. *Atmos.–Ocean,* **33,** 683–730.

Schmidt, G. A., and Coauthors, 2006: Present-day atmospheric simulations using GISS ModelE: Comparison to in situ, satellite, and reanalysis data. *J. Climate,* **19,** 153–192.

Schramm, J., M. M. Holland, J. A. Curry, and E. E. Ebert, 1997: Modeling the thermodynamics of a sea ice thickness distribution. 1. Sensitivity to ice thickness resolution. *J. Geophys. Res.,* **102,** 23 079–23 092.

Schweiger, A. J., 2004: Changes in seasonal cloud cover over the Arctic seas from satellite and surface observations. *Geophys. Res. Lett.,* **31,** L12207, doi:10.1029/2004GL020067.

——, R. W. Lindsay, J. R. Key, and J. A. Francis, 1999: Arctic clouds in multiyear satellite data sets. *Geophys. Res. Lett.,* **26,** 1845–1848.

Sellers, W. D., 1969: A global climatic model based on the energy balance of the earth–atmosphere system. *J. Appl. Meteor.,* **8,** 392–400.

Semtner, A. J., Jr., 1976: A model for the thermodynamic growth of sea ice in numerical investigations of climate. *J. Phys. Oceanogr.,* **6,** 379–389.

Shupe, M. D., and J. M. Intrieri, 2004: Cloud radiative forcing of the Arctic surface: The influence of cloud properties, surface albedo, and solar zenith angle. *J. Climate,* **17,** 616–628.

——, S. Y. Matrosov , and T. Uttal, 2005: Arctic cloud microphysics retrievals from surface-based remote sensors at SHEBA. *J. Appl. Meteor.,* **44,** 1544–1562.

——, ——, and ——, 2006: Arctic mixed-phase cloud properties derived from surface-based sensors at SHEBA. *J. Atmos. Sci.,* **63,** 697–711.

Stroeve, J. C., M. C. Serreze, F. Fetterer, T. Arbetter, W. Meier, J. Maslanik, and K. Knowles, 2005: Tracking the Arctic's shrinking ice cover: Another extreme September minimum in 2004. *Geophys. Res. Lett.,* **32,** L04501, doi:10.1029/2004GL021810.

Vavrus, S., 2004: The impact of cloud feedbacks on Arctic climate under greenhouse forcing. *J. Climate,* **17,** 603–615.

Wang, X., and J. R. Key, 2003: Recent trends in Arctic surface, cloud, and radiation properties from space. *Science,* **299,** 1725–1728.

Westwater, E. R., Y. Han, M. D. Shupe, and S. Y. Matrosov, 2001: Analysis of integrated cloud liquid and precipitable water vapor retrievals from microwave radiometers during the Surface Heat Budget of the Arctic Ocean Project. *J. Geophys. Res.,* **106,** 32 019–32 030.

Winton, M., 2006: Amplified Arctic climate change: What does surface albedo feedback have to do with it? *Geophys. Res. Lett.,* **33,** L03701, doi:10.1029/2005GL025244.

Zhang, J., and D. Rothrock, 2000: Modeling Arctic sea ice with an efficient plastic solution. *J. Geophys. Res.,* **105,** 3325–3338.

Zhang, M., W. Lin, C. S. Bretherton, J. J. Hack, and P. J. Rasch, 2003: A modified formulation of fractional stratiform condensation rate in the NCAR Community Atmospheric Model (CAM2). *J. Geophys. Res.,* **108,** 4035, doi:10.1029/2002JD002523.

Zhang, X., and J. E. Walsh, 2006: Toward a seasonally ice-covered Arctic Ocean: Scenarios from the IPCC AR4 model simulations. *J. Climate,* **19,** 1730–1747.

Zuidema, P., and Coauthors, 2005: An Arctic springtime mixed-phase cloudy boundary layer observed during SHEBA. *J. Atmos. Sci.,* **62,** 160–176.